

## SPACE ROBOTS

# Material remodeling and unconventional gaits facilitate locomotion of a robophysical rover over granular terrain

Siddharth Shrivastava<sup>1\*</sup>, Andras Karsai<sup>2\*†</sup>, Yasemin Ozkan Aydin<sup>2</sup>, Ross Pettinger<sup>3</sup>, William Bluethmann<sup>4</sup>, Robert O. Ambrose<sup>4</sup>, Daniel I. Goldman<sup>2†</sup>

Copyright © 2020  
The Authors, some  
rights reserved;  
exclusive licensee  
American Association  
for the Advancement  
of Science. No claim  
to original U.S.  
Government Works

Autonomous robots and vehicles must occasionally recover from locomotion failure in loosely consolidated granular terrain. Recent mobility challenges led NASA Johnson Space Center to develop a prototype robotic lunar rover Resource Prospector 15 (RP15) capable of wheeled, legged, and crawling behavior. To systematically understand the terradynamic performance of such a device, we developed a scaled-down rover robot and studied its locomotion on slopes of dry and wet granular media. Addition of a cyclic-legged gait to the robot's wheel spinning action changes the robot dynamics from that of a wheeled vehicle to a locomotor paddling through frictional fluid. Granular drag force measurements and modified resistive force theory facilitate modeling of such dynamics. A peculiar gait strategy that agitates and cyclically reflows grains under the robot allows it to "swim" up loosely consolidated hills. Whereas substrate disturbance typically hinders locomotion in granular media, the multimode design of RP15 and a diversity of possible gaits facilitate formation of self-organized localized frictional fluids that enable effective robust transport.

## INTRODUCTION

Planetary rovers face difficulties in soft soil during extraterrestrial exploration (1). NASA's Mars Exploration Rover Spirit became entrapped (the state of no forward motion due to excessive sinkage) in the low cohesion sulfate sands of Troy near the Gusev crater, resulting in the end of its mobility (2, 3). Modern Mars rovers like Spirit use six-wheeled rocker-bogie suspensions, which allow the rover to climb large solid obstacles (4, 5). Even so, these suspension systems cannot actively apply forces to the ground because their design passively enforces equal pressure among their wheels (6). Given the capability to individually apply active loads for each wheel, legged locomotion strategies, like those in terrestrial robots (7–9), could be a viable method for successful rover extraction from loosely consolidated substrates.

Soft, loose soil known as regolith covers large expanses of both lunar and Martian terrain (10). NASA's Lunar Crater Observation and Sensing Satellite mission revealed that regolith at the lunar poles is far less consolidated than in the regions explored during the Apollo missions (11, 12). Data from the Lunar Orbiter Laser Altimeter project show polar slopes up to a maximum of 35° (13, 14), near the angle of repose for the dry lunar regolith (15). In this dry granular regime, such steep slopes are sensitive to disturbance, are weak to stress and shear, and can readily avalanche (16, 17). These findings illustrate a risk of entrapment for future rovers exploring the lunar poles. To avoid this, active suspension and independent steering systems that can apply loads and lifts to individual wheels could enable a rover to execute various crawling behaviors to free itself and resume normal locomotion. Planetary rovers could thus navigate soft soil and traverse steep granular inclines, enabling them to access sites previously out of reach.

Granular media (GM), like regolith, poses a challenge for crawling locomotion because such substrates act like solids but flow when a yield stress is exceeded. The complex interactions between the media and an intruding body exerting stress can create a strongly coupled relation between the intruder's motion, the resistive force on it, and the terrain's state during and after intrusion (18, 8). Under locomotive shear, media may even be distributed into piles that act as obstacles for the locomotor. Disturbed GM presents challenges to locomotion by asymmetric piling or changing consolidation such that the GM is no longer homogeneous and predictable. Legged robots in previous studies met with considerable locomotive failure when reintruding into disturbed GM (19, 20), an effect exacerbated in granular slopes, where granular states weaken and avalanching can deform supporting structures (21). These systems demonstrate a feedback effect of speed reduction coupled to greater GM disturbance. To break this feedback, a locomotion method's dynamics must be insensitive to or even assisted by GM disturbance created by the locomotion.

As part of an early study for exploring for volatiles at the lunar poles, NASA's Johnson Space Center (JSC) participated in a mission study to provide mobility for carrying prospecting and processing instruments at the lunar poles, with the goal to verify orbital data with direct measurements of the volatiles. This project was called Resource Prospector. In 2015, the NASA Resource Prospector team built a prototype terrestrial robotic lunar rover called Resource Prospector 15 (RP15), a 300-kg rover that coupled conventional rotational wheel spin motion with a lifting and sweeping motion on each of its four appendages (Fig. 1A and movie S1). This drive train allowed the rover to use crawling strategies with its active suspension to traverse hills and escape entrapment where wheel spinning alone would fail (22). However, Resource Prospector was canceled as a mission concept in 2018; hence, little progress has been made on developing capabilities for RP15.

To discover terradynamic (8) locomotion principles for effective RP15 mobility and for the continued development of alternative rover designs, Georgia Institute of Technology and NASA JSC collaborated to create a scaled rover robot (Fig. 1B) called the Mini Rover that acts as a counterpart to RP15 (see fig. S1). Like RP15, the

<sup>1</sup>School of Mechanical Engineering, Georgia Institute of Technology, Atlanta, GA 30332, USA. <sup>2</sup>School of Physics, Georgia Institute of Technology, Atlanta, GA 30332, USA. <sup>3</sup>Jacobs Engineering Group, Houston, TX 77058, USA. <sup>4</sup>NASA Johnson Space Center, Software Robotics and Simulation Division, Houston, TX 77058, USA.

\*These authors contributed equally to this work.

†Corresponding author. Email: daniel.goldman@physics.gatech.edu (D.I.G.); akarsai3@gatech.edu (A.K.)

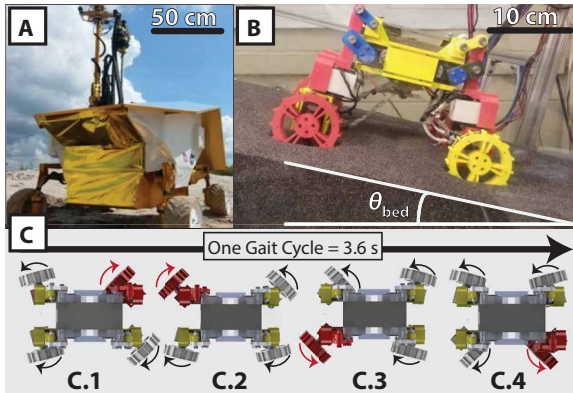


**Fig. 1. Prototype rovers with legged gait capabilities.** (A) NASA's RP15 prototype. (B) The Mini Rover resting on a bed of loosely packed poppy seeds on an incline of  $\theta_{\text{bed}} \approx 20^\circ$ . (C) Four top-view rendered snapshots of the Mini Rover executing a quadrupedal gait: an RS gait with no modulation. In the RS gait, all wheels except the one colored in red sweep toward the rear of the rover for 2.7 s. The sweep direction for each wheel in each snapshot is shown with the black arrows. Once the sweep is complete, the wheel begins the reset phase, where the wheel is colored in red. The Mini Rover lifts the resetting wheel with its four-bar linkage and rotates it  $90^\circ$  toward the front of the rover in 0.9 s. The reset direction for each wheel is shown in red arrows.

Mini Rover's locomotion combines aspects from both legged and wheeled robots, with appendages that intrude to provide propulsion (leg like) while also spinning to disturb the local terrain through shear (spin like; see fig. S2). Experiments in a controlled tilting bed of loosely packed GM (e.g., poppy seeds used for their low polydispersity, low cohesion, and inability to damage robotic components) allowed us to study its locomotion on slopes of GM with various open-loop gait patterns and strategies (Movie 1). Open-loop gaits have no feedback in their control logic, because each servomotor only receives position commands over time. These strategies are effective at extended time scales for a lower power draw in the robot, as the media has negligible rate dependence in its force response in the tested quasi-static regime (23). Because these gaits predominantly depend on geometrical shape changes of the rover rather than time-dependent dynamics, they are only force limited and remain viable for low-power robots and rovers. The core mechanism in these gaits is movement and remodeling of the local terrain.

## RESULTS

### Mini Rover locomotion in GM of varying slope

We first investigated an open-loop gait derived from tests of RP15's crawling capabilities at JSC. Previous studies showed that various open-loop strategies for granular slope climbing were sufficient if the locomotor's dynamics allowed it to repeatedly intrude into undisturbed media (21, 24). We implemented this gait on the Mini Rover (Fig. 1C) by cyclically sweeping rearward with three appendages while one appendage lifted to disengage from the medium and also spinning all four wheels at a constant rate of 2.1 rad/s. This gait is classified as a quadrupedal rotary sequence (RS) gait with regard to its foot placement (25), which cycles around the rover's locomotion appendages. In Fig. 1C, the RS gait has a time interval between each snapshot of 0.9 s. The wheels each have a radius of  $R = 4.2$  cm and 15 grousers evenly spaced along the rim, so at a rotational speed of 2.1 rad/s, each wheel intrudes about five grousers per s into the



**Movie 1. Research motivation, summary of locomotion strategies, and hill climbing through terrain remodeling.**

GM. We chose this wheel spin speed to agitate the local terrain multiple times per RS gait sweep, but when compared with an effect of gravity, the wheel spin is relatively slow. A comparable rate effect from gravitational acceleration of  $\sqrt{g/R} \approx 15.3$  [1/s] is larger than the grouser intrusion rate. Because gravity is the larger rate effect in the GM, grains do not enter freefall, and grain-grain contact is overall maintained. The wheel spins are considered “fast enough” for repeatedly disturbing the GM but not so fast that they dominate the terrain's acceleration over gravity.

We tested the RS gait's dynamics against wheel spinning alone by placing the Mini Rover in the granular test bed, having it spin its wheels for 30 s, and then executing the cyclic RS gait for 60 s (see fig. S3 and movies S2 and S3). Figure 2A shows the displacement versus time for these trials at  $\theta_{\text{bed}} = 0^\circ$ . In the initial spin-only phase, the wheels increasingly slip and sink, which leads to eventual entrapment. For the Mini Rover in loose poppy seeds, “wheel spin only” strategies resulted in entrapment for all tested  $\theta_{\text{bed}} \geq 0^\circ$ , because the Mini Rover's deep sinkage created too much granular drag for effective wheel traction. However, once the RS gait began, the rover restarted locomotion at a speed comparable to that before entrapment. The speed attained with the RS gait was insensitive to the depth of the rover wheels in the GM (see fig. S4), because the Mini Rover will sweep against the terrain to generate motive force. Because the rover's sinkage oscillates over time during the RS gait, the rover also generates a lift force from its sweeping to push itself out of entrapment, an effect observed in GM locomotion by previous studies (26). This locomotion paradigm contrasts with the traditional relationship between slip and sinkage for wheeled vehicles (27) and instead behaves more like a locomotor paddling through a self-organized rate-independent frictional fluid (24, 28).

The Mini Rover's locomotion ability is not limited to flat terrains; the RS gait enables motion after entrapment on granular slopes  $\theta_{\text{bed}}$  of up to  $15^\circ$  (Fig. 2B). For each tested bed angle  $\theta_{\text{bed}}$ , the rover achieves a different equilibrium speed for the RS gait when climbing hills with differing slopes. As slope increases, gravity gains a force component equal to  $mgsin(\theta_{\text{bed}})$  pulling the rover rearward, along with the grains losing resistive strength and avalanching more easily (16, 21, 29). The robustness of the RS gait in climbing loosely consolidated slopes motivated investigation of the individual dynamics of the RS gait's different subsystems: wheel spinning, lifting, and sweeping. We performed locomotion trials at  $\theta_{\text{bed}} = 15^\circ$  with different subsystems disabled, along with the regular RS gait described before as a control (Fig. 2C). Disabling any one of the three subsystems produced

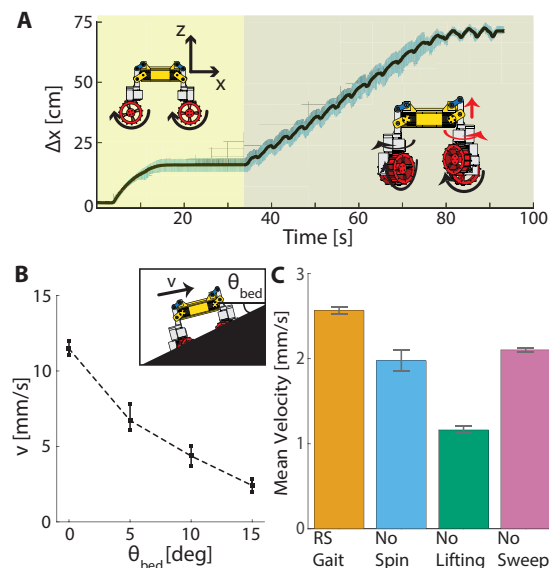


**Fig. 2. Robustness and performance of the rotary sequence gait.** (A) Horizontal displacement over time of the Mini Rover at rest for 5 s using wheel spin only on a  $0^\circ$  slope of loose poppy seeds for 30 s and then executing the RS gait described in Fig. 1C for 60 s. Data shown are means  $\pm$  SD for seven runs. The time interval shaded yellow from 0 to 35 s is the “wheel spin phase,” and shaded orange from 35 to 95 s is the “RS gait” phase. The Mini Rover reaches the end of the test bed near the 80-s mark. (B) Mean  $\pm$  SD velocities going uphill of the RS gait shown in (Fig. 1C) for different granular slope angles, varying the  $\theta_{\text{bed}}$  in (Fig. 1B), with seven trials for each bed angle. (C) Mean  $\pm$  SD average velocity over seven trials each in the steady state of the RS gait on a  $\theta_{\text{bed}} = 15^\circ$  poppy slope, with various subsystems of the gait disabled.

a lower mean velocity for the slope climbing. Disabling the motion was the most detrimental to the forward velocity. By not lifting the wheels during the reset sweeps of the RS gait, the wheels did not disengage with the GM and pushed the rover rearward, decreasing its mean velocity. Disabling the sweeping subsystem reduced the granular volumes encountered and transported by each locomotor appendage. The wheels oscillate purely vertically, which temporarily escapes entrapment and avalanches small amounts of media rearward during intrusion due to wheel spin. Last, disabling the wheel spin subsystem resulted in an  $\approx 20\%$  speed decrease. Compared to the sweeping subsystem, the wheel spin requires less power.

### Single appendage tests and RFT modeling

To develop an understanding of these phenomena, we next isolated the multiappendage Mini Rover locomotion system to a single locomotor appendage. We mounted a replica of a Mini Rover appendage that has both wheel spinning and sweeping capabilities to a six-axis force transducer (Fig. 3A). The entire system was mounted to a two-dimensional (2D) gantry driven by stepper motors in a tilting, fluidizing bed of poppy seeds. Approximately replicating the dynamics of the sweeping motion for a single locomotor appendage, we estimated the reaction forces felt by each appendage during the Mini Rover’s gaits. The appendage is forced at different fixed velocities  $v_x$  at set bed tilts  $\theta_{\text{bed}}$  chosen to match the RS gait results from Fig. 2B. To interpret the single-wheel system, the forcing speed  $v_x$  is set as a constant value matching the average gait speeds of Fig. 2B, whereas in the real Mini Rover system,  $v_x$  varies with time as the gait executes. The variable  $\theta_{\text{sweep}}$  in Fig. 3A represents the degree of sweeping rotation of the wheel (i.e., a  $-90^\circ$  offset from the wheel’s steering angle),

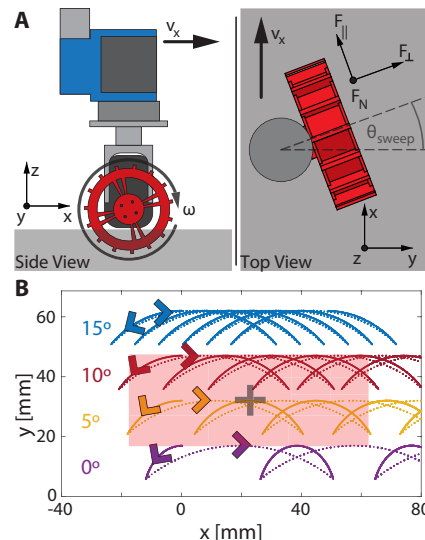


**Fig. 3. Isolation studies of single-wheel force response.** (A) Side view and top view schematics of the single-wheel gantry test bed. The Cartesian coordinate system  $\{x, y, z\}$  describes the world frame aligned with the test bed, whereas a local Wheel coordinate system  $\{F_{\parallel}, F_{\perp}, F_N\}$ , which rotates about  $z$  by  $\theta_{\text{sweep}}$ , defines the force responses parallel, perpendicular, and normal to the wheel at each sampled  $\theta_{\text{sweep}}$ . The wheel coordinate system rotates over time as the appendage executes its gait. (B) Top-down sketch of the sweeping wheel path input into the system in (A) at different  $\theta_{\text{bed}}$  values. The shaded rectangle is a projection of the top-down view of a single wheel for scale.

which varies over time as position commands are sent to the sweeping servomotor. We set the limits of this angle as  $\theta_{\text{sweep}} \in \left[-\frac{\pi}{4}, \frac{\pi}{4}\right]$  to match the RS gait’s sweeping motion, and this produces approximate motion paths that replicate the Mini Rover appendage’s trajectory through the bed of poppy seeds. Figure 3B shows a shaded rectangle as a top-down projection of a single wheel, with a crosshair in its center that moves along the trajectory paths. As  $\theta_{\text{bed}}$  increases and its coupled  $v_x$  decreases, the Mini Rover wheel tends to sweep a greater percentage of the same granular area for each gait cycle.

In the absence of a fully validated continuum model of complex granular interactions, a reduced-order empirical model called granular resistive force theory (RFT) can approximate the resistive forces on arbitrary intruders like our Mini Rover wheel by modeling the GM as a nondeforming isotropic medium and modeling the intruder as a rigid body composed of small plate elements (8). Because of the locality of granular force responses, it is possible to linearly add each small plate element’s respective resistance (calibrated via constant speed intrusion experiments) as a function of depth, orientation, and velocity. This sum of plate elements acts as a good approximation for the entire intruder for most intrusion states (30). Although RFT does not account for local terrain deformations in its force calculation, we will show how external agitations that reflow media to be locally homogeneous allow RFT to accurately predict force response as though the medium was fixed in place. This reflow of the GM allows accurate calculation of the force responses of the Mini Rover’s RS gait.

An entrapped Mini Rover in flat GM has an RS gait of  $v_x = 0$  mm/s and  $\theta_{\text{bed}} = 0^\circ$ , where the appendage is repeatedly sweeping through the same granular volume. The force transducer is mounted to the sweeping actuator, so its orthogonal coordinate system measures forces parallel, perpendicular, and normal  $\{F_{\parallel}, F_{\perp}, F_N\}$  to the wheel’s

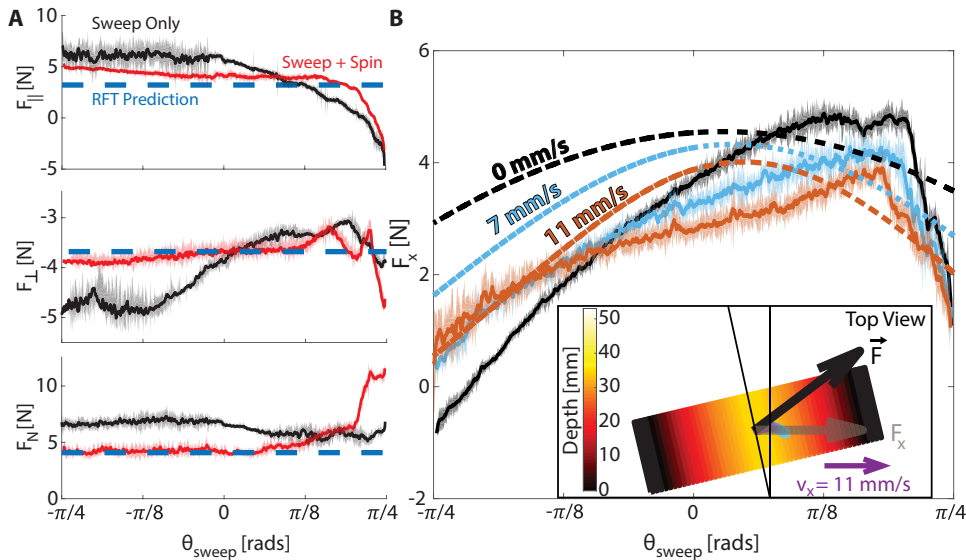


**Fig. 4. Single-wheel force response in stationary versus moving frames.** (A) For  $v_x = 0$  mm/s and  $\theta_{bed} = 0^\circ$ , force components for a stationary RS gait sweep rearward with wheel spin off versus wheels spinning at 2.1 rad/s. RFT calculation of the resistive forces for this trajectory gives flat force response curves with respect to  $\theta_{sweep}$ , because of cylindrical symmetry about the  $z$  axis. (B) For  $\theta_{bed} = 0^\circ$ , varying  $v_x$  in the gantry system (Fig. 2A) varies the drawbar force curves with respect to sweep angles. Experiments in solid lines, mean  $\pm$  SD across 20 sweeps in the steady state, and wheel spinning at 2.1 rad/s. Inset: 3D RFT simulation diagram for  $v_x = 11$  mm/s.

orientation, which depends on the current  $\theta_{sweep}$ . With  $v_x = 0$ , a stationary rotational axis of symmetry about  $z$  lets us interpret the force components with only the single variable  $\theta_{sweep}$ . This allows a 2D calculation of the expected forces on the sweeping intrusion geometry. We used RFT to calculate the expected values of the three force components for the sweeping wheel geometry. Figure 4A shows the RFT predictions along with the experimental mean and the SD of these force components more than 20 rearward gait sweeps each (i.e., from  $\theta_{sweep} = \pi/4$  to  $\theta_{sweep} = -\pi/4$ ) in a steady state with the wheel not spinning versus the wheel spinning at 2.1 rad/s. These trials reveal how wheel spinning might create the appreciable speed improvement seen in Fig. 2C. Force data show that spinning the wheel during the sweep produces flatter force responses that are more predictable from RFT, because the wheel spinning reflows local grains and homogenizes the local frictional fluid by actively avalanching local mounds (see movie S4). Unlike traditional wheeled locomotors that gain motive force by shearing terrain under pressure rearward with their wheels (27), the Mini Rover in the RS gait uses its wheels chiefly as agitators, while gaining most of its motive force from the sweeping motion. Adding agitation to the local terrain, the granular mound interactions that cause deviations from simple RFT-like force response are smoothed out.

**Measuring and modeling motive forces**

A primary force of interest in Fig. 4 is  $F_x$  [the “drawbar” force in the vehicle mechanics literature (31)], because this represents the motive force that the Mini Rover generates with one appendage during its RS gait. For nonzero  $v_x$ , there is no stationary axis of symmetry about  $z$ , so we transform the force components into the gantry coordinates  $(x, y, z)$  with a rotation matrix about  $z$  by the time-dependent  $\theta_{sweep}$ . We can also approximately extend the RFT calculation to three dimensions via a similar set of transforms for each tested  $v_x$ . Figure 4B

shows the RFT predictions for three chosen  $v_x$  as dashed lines along with the corresponding experimental force data. RFT predicts higher net  $F_x$  as  $v_x$  decreases due to more segments of the wheel having net rearward motion due to  $\theta_{sweep}$ . However, the experimental forces match best at the highest tested  $v_x$  and then diverge from the RFT calculation at lower  $v_x$ . Because RFT approximates the GM as a fixed volume in space, its predictive power is best for undisturbed, homogeneous regions of terrain. As  $v_x$  increases, the sweeping wheel encounters more undisturbed terrain per gait cycle (see Fig. 3B), so RFT gives a more accurate estimate. The data also suggest notable decreases for drawbar force for  $\theta_{sweep} < 0$  for all tested  $v_x$ , whereas RFT predicts a mostly symmetric response about  $\theta_{sweep} = 0$ . This is due to the wheel re-encountering previously disturbed terrain that was swept away by previous gait cycles, suggesting that gait strategies should seek to both sweep through undisturbed terrain if possible and actively reflow the local terrain to eliminate its

“memory” from previous gaits.

To further explore the Mini Rover’s motive forces, we performed experiments measuring the net drawbar force for different slopes using the RS gait (Fig. 5A and movie S5). After 30 s of wheel spin, the Mini Rover executed the RS gait for 215 s, while we measured its drawbar force with a strain gauge. The saturated force values near the end of each trial approximate the maximum possible drawbar force the Mini Rover can exert at a given  $\theta_{bed}$ , which we then compare to the sum of four gait appendages in the previous RFT calculation. Figure 5B shows each saturated experimental drawbar force from Fig. 5A compared with the corresponding potential drawbar from RFT. In this subfigure, the rover has periodicity in its force profile over a gait cycle that cycles through the reset phase for all four wheels. Meanwhile, the RFT is expected to have a quarter of the periodicity of one gait cycle, as it simply involves summing drawbar forces over four offset “isolated” wheels with no wheel-wheel interaction on unchanging flat terrain force at a constant  $v_x$ . In experiments, the rover also experienced oscillations over its gait cycle (see Fig. 2A), which added variation to the drawbar measurement due to its spring-like attachment to the sensor. For increasing  $\theta_{bed}$ , gravity increasingly pulled the Mini Rover rearward, so its sink and slip increased. Yet, because of the active reflowing of the Mini Rover’s wheel spin, local terrain was homogenized enough for RFT to predict net drawbar reasonably well on the basis of  $v_x$  alone, assuming a singular sinkage. Despite the kinematic differences, this RFT calculation estimates the mean drawbar for a range of bed angles.

**Robustness to appendage disability**

We also investigated the robustness of the RS gait by selectively disabling the sweeping motion of a single locomotor appendage. For Fig. 5C, we disabled the sweeping capability of the rear right

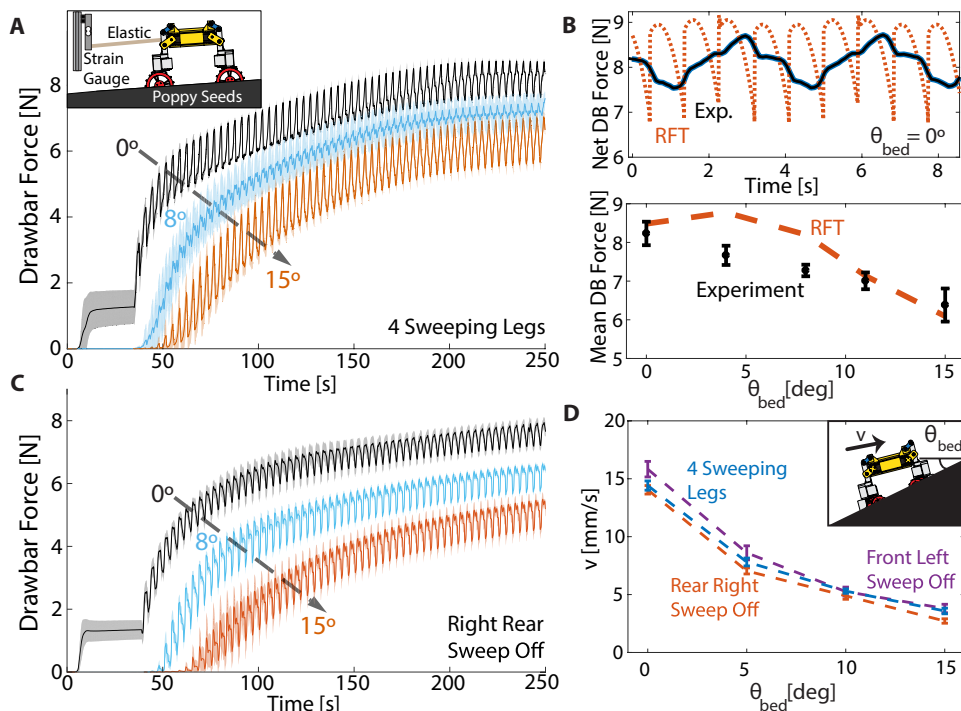


**Fig. 5. Propulsive forces in the Mini Rover's RS gait.** (A) Drawbar forces exerted over time by the Mini Rover using the RS gait with four sweeping legs up a bed of loosely packed poppy seeds at  $\theta_{bed} = [0^\circ, 8^\circ, 15^\circ]$  (inset shows experiment setup). Data shown are means  $\pm$  SD over seven trials for each value of  $\theta_{bed}$ . (B) Mini Rover saturated drawbar forces with the RS gait (top) experimental (solid) versus RFT-based calculation (dashed) over time for two gait cycles of the RS gait, summed over all four locomoting appendages. Bottom: Mean saturated drawbar pull with respect to  $\theta_{bed}$  for experiment (error bars) versus RFT calculation (dashed). (C) Drawbar forces exerted over time by the Mini Rover using the RS gait with three sweeping legs (with rear left leg sweeping disabled) up a bed of loosely packed poppy seeds at  $\theta_{bed} = [0^\circ, 8^\circ, 15^\circ]$ . Data shown are means  $\pm$  SD over seven trials for each value of  $\theta_{bed}$ . (D) Mean  $\pm$  SD velocities going uphill of the RS gait with four sweeping wheels versus selectively disabled sweeping wheels for different granular slope angles, varying the  $\theta_{bed}$  with seven trials performed for each bed angle.

appendage and measured the Mini Rover's drawbar pull for different granular slopes. The rear right wheel still executed its spinning motions during these trials, so it effectively acted as a passive agitator of contacted grains rather than an active sweeping component that exerts locomotive force. Compared to Fig. 5A, the rover exerted lower net drawbar force over time for all tested slopes. Because each appendages' sweeping motion is the primary generator of drawbar force, we expect such a force reduction. The Mini Rover made progress with one of its rear wheel's sweeping disabled and exerted an increasing drawbar force through the RS gait with only three sweeping legs. We then removed the drawbar apparatus and tested the unburdened rover's performance on various slopes as in Fig. 2, again with the rear left appendage's sweeping disabled. Our results in Fig. 5D show that the RS gait's velocity was only slightly reduced by this handicap. Even on the steeper slopes, the three-legged trials maintained similar displacement profiles to the four-legged trials, albeit at a lower speed. Because the disabled sweeping wheel continues to spin to fluidize local grains, we hypothesized that the other appendages were still able to function normally in the locally agitated medium. Another set of trials disabled the front left appendage's sweeping motion, and the translational velocities of the unburdened rover even surpassed that of the four appendage trials on some slopes. Along with Fig. 2C, this result showcases the robustness of the RS gait's locomotion mechanism to component

failure, along with potential for future optimizations for the gait performance.

### Measuring motive force of RP15

To validate our laboratory tests of the Mini Rover, we also performed drawbar tests with the RP15 rover at NASA JSC to compare the RS gait versus wheel spinning alone (Fig. 6A). Because of technical issues with the NASA rover, we conducted RP15 tests with only three operational sweeping leg actuators. We were also only able to conduct tests of RP15 on a flat, moist, sand bed because of constraints in the test bed environment. However, despite these differences from laboratory tests of the Mini Rover, we observed an increase in motive force in the RS gait as opposed to wheel spinning only (Fig. 6A), same as the laboratory results. Like the Mini Rover it inspired, RP15 creates a marked drawbar advantage using its active suspension via crawling gaits over traditional wheeled locomotion (see movie S6). This strategy can increase drawbar pull without large decreases in rover velocity (32). We also performed drawbar experiments on the Mini Rover that imitated the constraints of the RP15 tests, including disabling the sweeping mechanism of one Mini Rover appendage. Drawbar tests for the Mini Rover using the RS gait in moist 20/40 gradation sand (with a 1.8% water mass-to-dry GM mass percentage) yielded similar results to the wet sand trials with RP15 (Fig. 6B and movie S7). The wet GM has a very different rheology from dry GM because of its high cohesion, force saturation length scales, and high critical angle, making it inaccurate to model with dry substrate RFT (33). However, the RS gait still increased the Mini Rover's drawbar pull in this differing rheology. The legged RS gait with wheel spin is thus robust to varying terrain types and even component failure.

### Rear rotator pedaling and slope reconfiguration

The RS gait developed for RP15 is robust for many scenarios but cannot successfully climb granular slopes near the critical angle of avalanching. For  $\theta_{bed} > 20^\circ$ , the RS gait generates unpredictable behavior—from roll over to pronounced yaw. To climb these steeper slopes in the laboratory, we developed a specialized hill-climbing gait that we refer to as "rear rotator pedaling" (RRP; see Fig. 7A). Like the RS gait, the Mini Rover lifts and resets the wheel colored red at each snapshot of Fig. 7A, now alternating between only the rear wheels. Each wheel spins at 2.1 rad/s during the RRP gait, including the front wheels. These motions generate a periodic yaw oscillation of the rover. After spinning wheels for 30 s to embed the Mini Rover in the media, once the RRP gait initiates (node 1 in Fig. 8A), if  $\theta_{bed} > 20^\circ$ , then the rover initially slides backward until a sufficient mound develops behind its rear wheels, which prevents further rearward sliding (node 2) and acts as a buffer the rear wheels can

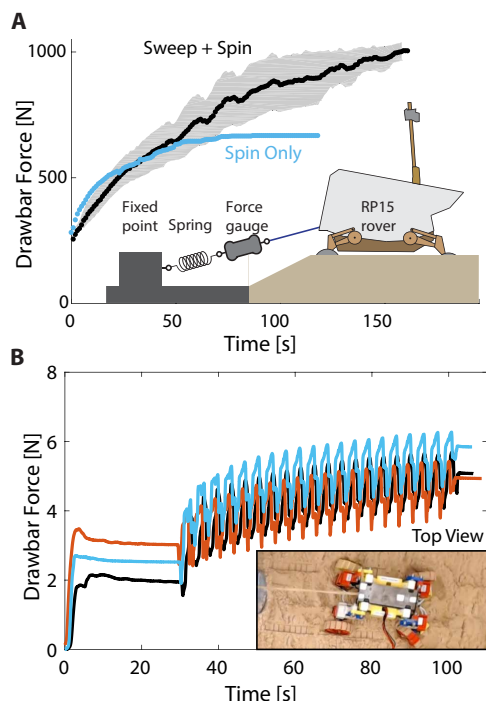


**Fig. 6. Propulsive forces of RP15 and Mini Rover in wet granular media.** (A) Drawbar forces exerted over time by RP15 during tests in a bed of moist sand at JSC (diagram shows experiment setup). Blue data points show one trial of RP15 executing a wheel spin motion for 120 s, and black data show the means  $\pm$  SD for three trials of RP15 executing an RS gait for 170 s. (B) Drawbar force versus time for three moist sand RS gait drawbar trials of the Mini Rover. Each different colored line represents a different trial. The Mini Rover generates increasing drawbar force with the RS gait even with one appendage sweeping mechanism disabled and in a much more cohesive substrate than the dert GM trials with three active wheels. Inset: Mini Rover in a bed of moist sand exerting drawbar forces with the RS gait in a bed of moist sand (top view). Qualitatively, the grouser-sand interaction appears to closely mirror the RP15 experiments (e.g., the grousers became smooth as the wheels spin and sand aggregates between the grousers.)

push on to move forward. After this initial mound is generated, the rover climbs the slope at constant speed (Fig. 8A). Although RRP locomotes more slowly than the RS gait at  $\theta_{\text{bed}} = 0$ , the RRP gait outpaces the RS gait for all other tested slopes, managing to climb hills of  $\theta_{\text{bed}}$  that the RS gait could not (Fig. 7B).

The RRP gait's performance arises from a stable granular conveyance action that develops along the Mini Rover's long axis. As the front wheels spin and shear the steep granular slope at the rover's front, the material avalanches downhill (29) and is transported between the rover's front and rear wheels to an "intermediate mound" (IM) closer to the rear wheels' reach (see Fig. 7C, diagram). The yaw oscillation of the rover body pushes media in the IM rearward where the RRP gait's sweeping reaches and pushes it into a rear mound to apply a net propulsive force. On steep slopes of  $\theta_{\text{bed}} > 20^\circ$ , over time, the gait will dynamically reconfigure an initially insurmountable slope through avalanching and granular conveyance to create a terrain profile it can climb (Fig. 7C, fig. S5, and movie S8). The rover requires a large enough rear mound to provide propulsive force, and the IM arises from the granular conveyance action. This dynamic reconfiguration allows the Mini Rover to "swim" uphill in the agitated frictional fluid created by its wheel spin. If the front wheel spin is disabled in the RRP gait (Fig. 8A, node 1), then the rover will con-

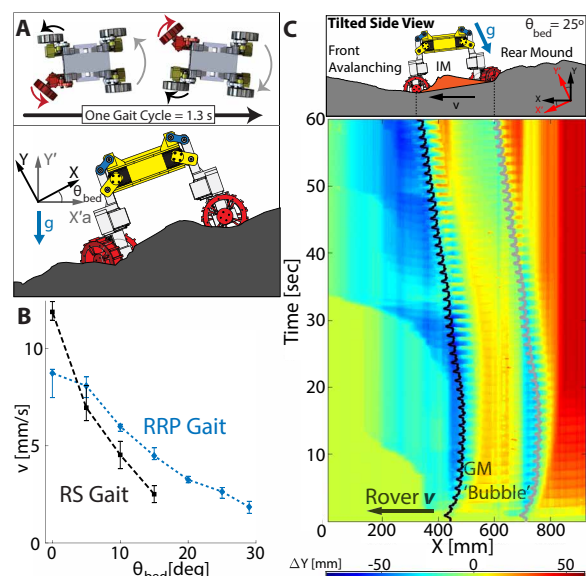


**Fig. 7. Steep granular slope climbing via dynamic remodeling with an RRP gait.** (A) Top: Two top-down snapshots showing a RRP gait with no modulation, with a time interval between each snapshot of 0.65 s. In the RRP gait, the rear wheel colored in white sweeps toward the rear of the rover up to  $45^\circ$ . The sweep direction for each wheel in each snapshot is shown in black arrows. Once the sweep is complete, the wheel begins the reset phase, where the wheel is colored in red. The Mini Rover lifts the resetting wheel with its four-bar linkage and rotates it  $45^\circ$  toward the front of the rover. Bottom: Side-view illustration of the Mini Rover climbing a hill of GM using the RRP gait. (B) Mean velocities going uphill of the RS and RRP gaits shown in Fig. 1C and (A), respectively, for different granular slope angles ( $\theta_{\text{bed}}$ ). Data shown are means  $\pm$  SD over seven trials for each angle. There is overall less variance in the RRP gait's mean velocity over multiple trials than the RS gait's, because RRP exhibits a more predictable and stable speed at steep  $\theta_{\text{bed}}$ . (C) Height difference color map of the GM profiles over time as the Mini Rover executes the RRP gait on a  $25^\circ$  granular slope, with the spatial components in the tilted bed coordinate system ( $x, y$ ) shown in (A). A black line indicates the rover's front wheel's position over time, and a gray line indicates the rear wheel's position over time. The rover carries the IM as a bubble of GM between these dots as it locomotes forward, maintaining a net flux of GM from the rover's front wheels to the rear mound.

tinue to slide backward until it encounters the rear test bed wall (node 2') and then push off that boundary to slowly climb up the slope (node 3'). Disabling the granular conveyance mechanism causes failure in the RRP gait for steep slopes, showing that avalanching through local agitation is necessary to climb (see movie S9).

For trials where  $\theta_{\text{bed}} > 20^\circ$ , the rover carries the IM as a "bubble" of granular volume as it locomotes forward, showing how the granular conveyance mechanism maintains a net flux of media across the rover's length. These steep slopes require this IM to increase in volume before the rover will gain any net forward locomotion, whereas rover speed is mostly insensitive to the IM size at shallower slopes (Fig. 8B). Insufficient IM volume causes the rover to slide backward until the granular conveyance process saturates to a steady state, at which point the rover maintains a steady speed and IM volume over time (Fig. 8).

## DISCUSSION

Our results demonstrate that robots with unconventional legged gaits and appropriate local fluidization via wheel spinning can use the

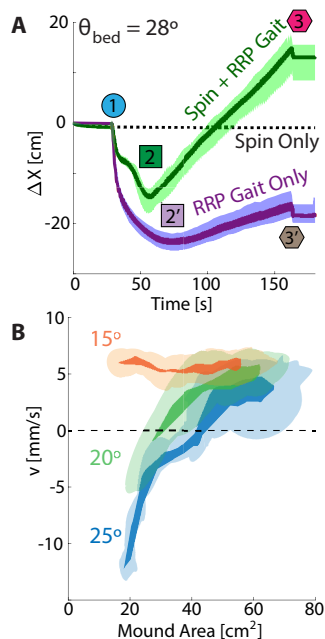


**Fig. 8. Performance and granular transport mechanisms for the RRP gait.** (A) Uphill displacement over time of Mini Rover using the RRP gait to climb a 28° granular incline. Turning off the wheel spinning or sweeping components of the RRP gait causes failure to climb. Data represent means  $\pm$  SD for seven trials for each condition. The numbered nodes represent key events in the rover's climbing dynamics, where the rover initiates the RRP gait at node 1, ends slide back and begins forward progress once the rear mound has formed at node 2, and ends the RRP gait at node 3. (B) Bivariate boxplot of the 2D-projected area of the IM that forms between the two wheels of the Mini Rover as it climbs with RRP (see diagram in Fig. 7C) with respect to the Mini Rover's uphill velocity, with 13 total trials of 50 s each over three values of  $\theta_{\text{bed}}$ . The solid colors are the boundary of mean trajectories over time for these two variables. At each mean trajectory point, the covariance matrix of velocity and mound area at that time stamp creates an error ellipse centered at  $\mu$  (mean) with dimensions  $\pm 1\sigma$  (SD). The union of the set of error ellipses for each mean trajectory point gives the shaded regions, representing the variance between trials for each group of  $\theta_{\text{bed}}$ .

loose consolidation of GM to their advantage by creating self-organized localized frictional fluids. This loose consolidation in GM traditionally causes entrapment for wheeled and legged robots (19). Both RP15 and the Mini Rover increased their drawbar pulls when they switched from wheeled locomotion to open loop gaits that agitate the local media. Creating a homogeneous terrain profile through this agitation erases terrain memory effects that hinder locomotion, creates force uniformity, perturbs material to avalanche into more advantageous terrain, and allows force calculation via RFT.

Although terrain reconfiguration with legged gaits appears effective for noncohesive media, future studies must consider that planetary regolith is often very cohesive and polydisperse. Cohesive regolith will likely not avalanche and flow as easily as the noncohesive poppy seeds in this study. The drawbar experiments for both RP15 and the Mini Rover in wet sand (Fig. 6) exhibited some visible terrain reconfiguration due to the rovers' high slip, as mounds of granular material formed behind the spinning wheels. However, these mounds appeared to be more loosely packed than the dry poppies due to their high cohesion. The grain-grain cohesion in flat terrain hinders the desired advantageous avalanching and reconfiguration that is key to the gait. We hypothesize that sloped terrain may actually assist by

introducing a gravity component downhill. Gravity could then avalanche the grains to help the rear mounds form and consolidate, rather than the rover scooping out a hole around the wheels that ensures entrapment. Future studies and experiments could examine how these gaits perform on sloped cohesive terrain. Investigating these gaits on more inhomogeneous GM would also be interesting, because the rate of terrain reconfigurations may change according to the local media's constitutive particles.

Certain modern rover designs, such as the European Space Agency and Roscosmos' Rosalind Franklin, already incorporate up to three degrees of freedom in active actuation per wheel (34), allowing the rover's locomotion subsystem to adjust its stance for crawling over obstacles. More traditional control (35) and wheel design (36) approaches are still effective, but the capability to perform active legged behaviors as well could enable future exploration of steep terrains (37) inaccessible to other planetary rovers. Fluidized granular beds and other improved substrate creation systems on Earth will be critical for evaluating the physical principles of legged climbing in these larger robots. RP15 and future rovers can use these principles to guide both robot and motion design. With different appendages, sensors, and actuation schemes, perhaps such dynamical terrain modification can be applied to more diverse substrates. In future studies, closing the control loop with additional local terrain sensing could further terradynamic capabilities of rover exploration.

## MATERIALS AND METHODS

### Mini Rover robot experiments in dry granular media

To systematically evaluate the performance impact of varying the gait and to understand the dynamics of rover performance, we developed a robophysical model rover inspired by RP15's morphology and movement. This model rover (Mini Rover) is 30 cm in length, 23 cm in height, and 20 cm in width. All rover body and appendage components were made of 3D-printed acrylonitrile butadiene styrene plastic. The rover has four appendages (an appendage is a term used to classify a rover subassembly containing the lifting, sweeping, and wheel spinning motors) that achieve lifting motion through a four-bar linkage and the sweeping and spinning motions through direct motor connections. Each appendage is operated by three separate Dynamixel AX-12 servoactuators. The appendages were assembled using various screws to fasten the four-bar linkages and servos and a series of radial and ball bearings to minimize frictional forces. 3D-printed hollow-body grouser-spoked wheels (8.7 cm in diameter) were attached to wheel spinning motors. All assembly components were rigid and had negligible elastic deformation. Reflective markers were placed on the body to enable the OptiTrack system to capture rover kinematic data. A steel bar attached to the top of the rover enabled an electromagnet on the automated gantry to lift and reset the rover for each experiment.

All Mini Rover experiments were conducted in a semiautomated test bed full of our selected GM (dry poppy seeds) capable of tilting to change the bed incline, air fluidization of GM, capture of rigid body kinematic data, and precise resets of the robot through an electromagnet on a gantry system. Bed tilt was adjusted via two Firgelli linear actuators. The granular bed's fluidization mechanism blows air to fluidize the poppy seeds and reset the granular state as discussed in (38). Four OptiTrack motion capture cameras were mounted on the tilting frame (the same frame of reference as the

Mini Rover) above the granular bed and captured kinematic data of reflective markers attached to the Mini Rover at 60 frames per s.

The quadrupedal gait used for small  $\theta_{\text{bed}}$  is the RS gait with no modulation. A series of four SolidWorks renders viewed from the top of the Mini Rover looking downward illustrate this gait in Fig. 1C. At the figure's top is the arrow of time/sequence order, showing that one gait cycle takes a total of 3.6 s to execute. The Mini Rover is drawn moving rightward. When executing its RS gait, the Mini Rover performs the same sequence of two-phase ("sweep" and "reset") motions to each of its four wheels in a counterclockwise order, beginning with the front left wheel in the C.1 frame being in the reset phase. In the RS gait, all wheels except the one colored in red sweep toward the rear of the rover for 2.7 s. The sweep direction for each wheel in each snapshot is shown with the black arrows. Once the sweep is complete, the wheel begins the reset phase, where the wheel is colored in red. The Mini Rover lifts the resetting wheel with its four-bar linkage and rotates it 90° toward the front of the rover in 0.9 s. The reset direction for each wheel is shown in red arrows. The Mini Rover then sets the wheel down to its original position, the reset phase completes, and wheel returns to the sweep phase. The entire gait cycle is cyclic, so the motion repeats from C.1 after C.4 is complete. Each wheel is always offset in time and position from the others. During an RS gait, each wheel is also spinning at 2.1 rad/s.

The high-incline experimentation quadrupedal gait is the RRP gait with no modulation, with a time interval between each snapshot of 0.65 s (see Fig. 7A). Like the RS gait, the Mini Rover lifts and resets the wheel colored in red at each snapshot but now alternates between only the back wheels. During a normal RRP gait, each wheel is also spinning at 2.1 rad/s, including the front wheels. This gait develops a lateral oscillatory behavior for the Mini Rover.

Any usage of the term "gait" in the main text implies either RS or RRP gaits. In a traditional experimental cycle, the test bed angle ( $\theta_{\text{bed}}$  between 0° and 30°), gait cycle quantity ( $\geq 0$  cycles), and the duration of wheel spinning before gait execution ( $\geq 0$  s) are set before trial initiation. The parameters of step frequency and wheel speed were constant for all trials shown in this paper. Once these experimental parameters for the gait have been set, the trial was initiated, and the rover wheels spun for a set time interval of 30 s. After this time interval, the wheels were sufficiently buried to be at the full slip condition, and the rover was entrapped within the granular substrate. The rover then executed the gait, enabling positive locomotion from the embedded state. After the rover stopped executing gait cycles, the trial concluded; the kinematic data from OptiTrack were imported to MATLAB and analyzed. The rover and granular terrain were then reset to their initial state through the automated gantry and bed fluidization, respectively.

To capture the drawbar experiment data, we fastened a Uxcell bar-type load cell to the bed frame. One end of an elastic tube was attached to the load cell and the other end to the rover. An HX711 load cell signal amplifier was used to process and feed the signal into a microcontroller. The microcontroller printed drawbar values at 11 Hz to a connected computer.

### Single-wheel gantry experiments

In Fig. 3A, a diagram details the single-wheel gantry test bed for testing granular force responses in the Mini Rover's locomotion. Two perpendicular rail systems hold a sweeping Dynamixel servomotor connected to a six-axis force/torque transducer (ATI Mini40), with its tool side connected to a wheel spinning Dynamixel servo,

which spins a wheel design copied from the Mini Rover. The system locomotes in a granular bed of poppy seeds, which fluidizes to a loose-packed state after every trial and can tilt up to 30° from horizontal like the granular bed described previously.

The left panel of Fig. 3A is a side view with the  $y$  axis of a Cartesian coordinate system out of the page. The gantry system is forced in the  $+x$  direction by a stepper motor coupled to a timing belt at a speed  $v_x$  at various granular bed tilts  $\theta_{\text{bed}}$ .  $v_x$  is chosen for each bed angle to approximate the actual Mini Rover speeds measured in Fig. 2B. The gantry is free to fall under its own weight during locomotion, simulating the normal force on the Mini Rover. Measurements with a scale gave 3.4 N (350 g) of normal force when the wheel rests on a solid surface. For all trials where wheel spinning was enabled, the wheel spun at  $\omega = 2.1$  rad/s.

To match a single wheel's RS gait period,  $\theta_{\text{sweep}}$  sweeps back from +45° to -45° in 2.7 s and then sweeps forward to reset from -45° to +45° in 0.9 s, as shown in Fig. 3B. All of the paths are represented by dots evenly spaced in time by 30 ms. The different colors represent different tilt angles and thus different commanded  $v_x$ . For bed tilt angles of 0°, 5°, 10°, and 15°,  $v_x$  was matched as 11.5, 6.7, 4.4, and 2.4 mm/s, respectively. These correspond to path colors (violet, yellow, crimson, and blue, respectively). Each path is drawn for a total of six gait cycles. The different  $v_x$  values are the only parameters that influence these; the sweeping period and amplitude were identical among all these paths. This motion command creates an arcing motion in space that has the wheel sweep the same granular area multiple times in its locomotion.

### Granular resistive force theory calculations

For Fig. 4A, the commanded sweeping motion describes a simple path through space that is symmetric about the  $z$  axis with  $v_x = 0$  mm/s. This cylindrical symmetry about the  $z$  axis of the force response allows a simple calculation through RFT, which is independent of  $\theta_{\text{sweep}}$ , giving a flat force response for all three force component plots, shown in the blue dashed lines in Fig. 4A. The RFT calculation approximates the single-wheel geometry as a narrow cylinder then projects to two dimensions. Once in 2D, we calculate the forces for a partially intruded cylinder with the dimensions of the Mini Rover wheel sweeping about the  $z$  axis using the techniques described by Li, Zhang, and Goldman (8). The depth was calibrated by matching the RFT wheel depth to the experimentally observed depth of the single wheel in video recordings of gantry experiments. We used the established RFT coefficients of loosely packed poppy seeds from the Li *et al.* paper (8) for all of our RFT calculations.

When  $v_x \neq 0$  mm/s, the cylindrical symmetry breaks, and a more complete three-dimensional RFT calculation is needed. For each set of experiments in Fig. 4B, we performed a quasi-3D RFT simulation that recreates the single-wheel gantry experiment geometry. This calculation decomposes the top view of Fig. 3A into a geometry of many adjacent small rectangles at depths dictated by the wheel sinkage. The wheel is still approximated as a narrow cylinder, but now, each subsegment has a more complex motion through space dictated by the test trajectories of Fig. 3B. The RFT calculation is then performed on this set of subsegments and summed to give the net resistive force. For the 3D RFT calculation, the wheel was modeled as a nongrousered solid cylinder with caps, with the sides of the wheel approximated as the flat faces of a cylinder. The force per plate calculation is performed by projecting the 3D problem into the  $xz$  plane as shown in the side view of Fig. 3A (left) and calculating

the resistive forces in the intruding 2D cylinder. We then approximate 3D RFT as being cylindrically symmetric, such that the resistive force vectors of the  $xy$  plane in Fig. 3A (plane parallel to granular surface) are exactly opposite to each subsegment's velocity vector (i.e.,  $\hat{\mathbf{F}} = -\hat{\mathbf{v}}$  in Fig. 3A, right). In this way, we neglect drag anisotropy by observing that most subsegments have velocity vectors mostly pointing toward the normal (i.e., overall  $\hat{\mathbf{v}} \cdot \hat{\mathbf{N}} > 0.5$ ) in their commanded motions. The forces in the  $xy$  plane are thus approximated by projecting the horizontal forces of each subsegment calculated from the diagram in Fig. 3A (left) into the proper  $xy$  velocity frame. The same method calculates the resistive forces to the two flat sides of the wheel, just with the normal vectors rotated 90°. The inset for Fig. 4B shows a simulation snapshot for  $v_x = 11$  mm/s, with a net force response vector that we then project onto the  $x$  axis to obtain the drawbar force at each  $\theta_{\text{sweep}}$  value. From experimental video, we estimate the single wheel to be buried about 35-mm deep at its deepest point, from which we can infer the depths for each wheel segment in the RFT calculation. The wheel's subsegments are colored by depth, with the hotter colors indicating deeper burial (up to 35 mm). A trailing series of dots near the wheel center also show the last 0.3 s of trajectory. These RFT simulations create the force curves represented by the dashed line curves in Fig. 4B.

For Fig. 5B, the RFT calculation results for each set of  $[\theta_{\text{bed}}, v_x]$  parameters from Fig. 4B were interpolated as functions of  $\theta_{\text{sweep}}$ . We then created four “virtual” wheels that had the gait sequence, timing, and trajectory of the RS gait to represent the four wheels of the Mini Rover, calculated the forces on each wheel with our interpolated RFT functions, and then summed the drawbar forces created by each virtual wheel to estimate the net drawbar force over time.

### RP15 experiments

We conducted experiments on RP15 (Fig. 1A) at JSC. RP15 dimensions are 140 cm in length, 200 cm in height, and 140 cm in width, with a mass of 300 kg. During our experiments, the rover had four operational driving wheels and three operational sweeping motors. As a result, only three appendages were able to execute the RS gait. A mechanical scale captured the drawbar force exerted by RP15. One end of the scale was fastened to the ground and the other to an elastic that was attached to the rear of RP15 (Fig. 6A). A Phoenix motion capture system captured the kinematic data of the rover via reflective markers placed on RP15.

Experiments with RP15 were conducted on moist sand. The moist terrain led to accumulation of compacted sand between the grouser spokes, changing the wheels' effective geometries to cylinders over time. RP15 would begin its experiment with only wheel spinning and then initiate the RS gait. A trial was concluded once RP15 could no longer locomote because of the saturation of drawbar force once it was at 100% slip. To reset the rover, the grousered wheels were excavated from entrapment, and the rover reversed its motion back to the initial starting position. We then pushed a device that aerated the wet sand to restore terrain homogeneity between experiments. Only the flat incline angle (0°) had experiments performed. An experiment with only wheel spinning motion was also conducted without any transition to the RS gait for comparison.

### Mini Rover robot experiments in wet granular media

To more directly compare the experimental conditions between RP15 and the Mini Rover, we also performed drawbar measurement experiments that replicated the conditions of RP15s drawbar trials.

We mixed 50 kg of sand and 0.9 liter of water to obtain a 1.8% water mass-to-dry GM mass ratio (33) and conducted drawbar trials for the Mini Rover with the RS gait. To replicate the failure of one of RP15s sweeping motor for one of the appendages, we also disabled the sweeping mechanism of one Mini Rover appendage for these trials. Only the sweeping mechanism for one appendage was disabled, whereas the lifting and wheel spinning actions remained active (see fig. S2). Between each drawbar trial, the sand was leveled and loosened by hand. Results of these trials are in fig. S5.

### RRP gait and dynamic reconfiguration

In Fig. 7C, a color map shows the GM profiles over time as the Mini Rover executes its RRP gait. This color map was generated by analyzing the video taken at the side view of the granular test bed over an entire RRP trial, with the Mini Rover hugging the side wall. The granular bed is tilted to some angle  $\theta_{\text{bed}}$ , and the camera is tilted as well such that the GM initially lies horizontal in the camera frame. The mound profiles at each moment in time were found by edge detection along with various postprocessing techniques to get accurate mound profiles. The mound changes over time were then subtracted from the grain level at  $t = 0$  s to obtain the height differences of the grain surface. In Fig. 7C, we have restricted the time dimension shown to between the start of the RRP gait and the end of RRP for clarity.

Figure 8B shows a bivariate boxplot of the emergent IM volume that forms between the two wheels of the Mini Rover as it climbs with RRP. This plot was generated by examining multiple videos of the type described for Fig. 7C, edge detecting the granular profile along with tracking the Mini Rover itself, then calculating the area of GM that lay between the two wheels' lowest points (see the inset of Fig. 7C). This mound area is a projection onto two dimensions of the approximate volume of the IM the Mini Rover carries with itself while climbing. In the mound area calculation, the mound profiles were median filtered across a time window of 0.3 s to help resolve false detections.

The plots shows three groups of data at different bed tilt angles (the independent variable): 15° (orange) consisting of five RRP trials, 20° (green) consisting of five RRP trials, and 25° (blue) consisting of three RRP trials. Each trial is synced in time with the other trials in its group. The time interval that each trial examines begins at marker 1 in Fig. 8A (when RRP begins) to 60 s after marker 1. This is so that the Mini Rover can reach a steady limit cycle but is far away in space from reaching the end of the granular bed. Because the trials for each data groups are synced in time, each trial's data can be compared with the other trials' data in the same group. This allows us to calculate the mean and covariance of each trial group and condense the parametric trajectories of each trial into an area plot. We calculated the means between all the trials for each group, which creates a mean trajectory for each bed angle through the mound area and velocity variable space. We took the boundary of this mean trajectory for each group and represented it as the solid colored area for each bed tilt group. At each mean trajectory point, we also calculated the covariance matrix for that observed timestamp and then created an error ellipse about that mean trajectory point (confidence interval is 0.68, the first SD). This gives us a representation of the variance between trials. We then took the union of the entire set of error ellipses for each group and plotted the error area as a lightly shaded region for each group's color.

### SUPPLEMENTARY MATERIALS

robotics.sciencemag.org/cgi/content/full/5/42/eaba3499/DC1

Fig. S1. Engineering sketches of the Mini Rover.

Fig. S2. Diagram of rover appendage actuations.  
 Fig. S3. Granular experimentation bed and gantry.  
 Fig. S4. Mini Rover RS gait velocity and sinkage profiles.  
 Fig. S5. Dynamic reconfiguration with the RRP gait on various slopes.  
 Movie S1. RP15 climbs granular mound with the RS gait.  
 Movie S2. Mini Rover using RS gait on a flat poppy seed bed.  
 Movie S3. Mini Rover RS gait trial in granular experimentation bed.  
 Movie S4. Single-wheel gantry trial of spin and sweep motion.  
 Movie S5. Mini Rover RS gait trial measurement of drawbar force.  
 Movie S6. Drawbar force measurements of RP15 prototype rover.  
 Movie S7. Mini Rover RS gait drawbar force measurement in wet sand bed.  
 Movie S8. Mini Rover RRP gait on sloped poppy seed bed.  
 Movie S9. Comparison of Mini Rover RRP gait with wheel spin enabled versus disabled.

## REFERENCES AND NOTES

- B. Schäfer, A. Gibbesch, R. Krenn, B. Rebele, Planetary rover mobility simulation on soft and uneven terrain. *Vehicle Syst. Dyn.* **48**, 149–169 (2010).
- R. E. Arvidson, J. F. Bell III, P. Bellutta, N. A. Cabrol, J. G. Catalano, J. Cohen, L. S. Crumpler, D. J. Des Marais, T. A. Estlin, W. H. Farrand, R. Gellert, J. A. Grant, R. N. Greenberger, E. A. Guinness, K. E. Herkenhoff, J. A. Herman, K. D. Iagnemma, J. R. Johnson, G. Klingelhöfer, R. Li, K. A. Lichtenberg, S. A. Maxwell, D. W. Ming, R. V. Morris, M. S. Rice, S. W. Ruff, A. Shaw, K. L. Siebach, P. A. de Souza, A. W. Stroupe, S. W. Squyres, R. J. Sullivan, K. P. Talley, J. A. Townsend, A. Wang, J. R. Wright, A. S. Yen, Spirit Mars rover mission: Overview and selected results from the northern home plate winter haven to the side of scamander crater. *J. Geophys. Res.* **115**, E00F03 (2010).
- J. L. Callas, Mars exploration rover Spirit end of mission report (technical report, California Institute of Technology, Jet Propulsion Laboratory, 2015).
- D. B. Bickler, *The New Family of JPL Planetary Surface Vehicles* (Missions, Technologies, and Design of Planetary Mobile Vehicles, 1993), chap. 19, pp. 301–306.
- K. Yoshida, H. Hamano, Motion dynamics of a rover with slip-based traction model, in *Proceedings of the IEEE International Conference on Robotics and Automation* (catalog no. 02CH37292, IEEE, 2002), vol. 3, pp. 3155–3160.
- R. Lindemann, C. Voorhees, Mars Exploration Rover mobility assembly, design, test, and performance, in *Proceedings of the IEEE International Conference on Systems, Man and Cybernetics* (IEEE, 2005), pp. 450–455.
- J. Aguilar, T. Zhang, F. Qian, M. Kingsbury, B. McInroe, N. Mazouchova, C. Li, R. Maladen, C. Gong, M. Travers, R. L. Hatton, H. Choset, P. B. Umbanhowar, D. I. Goldman, A review on locomotion robophysic: The study of movement at the intersection of robotics, soft matter and dynamical systems. *Rep. Prog. Phys.* **79**, 110001 (2016).
- C. Li, T. Zhang, D. I. Goldman, A terradynamics of legged locomotion on granular media. *Science* **339**, 1408–1412 (2013).
- Y. Ozkan-Aydin, J. M. Rieser, C. M. Hubicki, W. Savoie, D. I. Goldman, *Robotic Systems and Autonomous Platforms*, S. M. Walsh, M. S. Strano, Eds., Woodhead Publishing in Materials (Woodhead Publishing, 2019), pp. 109–127.
- G. Ishigami, A. Miwa, K. Nagatani, K. Yoshida, Terramechanics-based model for steering maneuver of planetary exploration rovers on loose soil. *J. Field Robot.* **24**, 233–250 (2007).
- P. Tompkins, R. Hunt, M. D’Ortenzio, K. Galal, D. Foreman, J. Munger, M. Shirley, J. Strong, R. Barber, E. Drucker, Flight Operations for the LCROSS Lunar Impactor Mission, in *SpaceOps 2010 Conference* (American Institute of Aeronautics and Astronautics, 2010); <https://arc.aiaa.org/doi/10.2514/6.2010-1986>.
- P. H. Schultz, B. Hermalyn, A. Colaprete, K. Ennico, M. Shirley, W. S. Marshall, The LCROSS cratering experiment. *Science* **330**, 468–472 (2010).
- M. A. Rosenburg, O. Aharonson, J. W. Head, M. A. Kreslavsky, E. Mazarico, G. A. Neumann, D. E. Smith, M. H. Torrence, M. T. Zuber, Global surface slopes and roughness of the Moon from the Lunar Orbiter Laser Altimeter. *J. Geophys. Res.* **116**, 10.1029/2010JE003716 (2011).
- M. A. Kreslavsky, J. W. Head, The steepest slopes on the Moon from Lunar Orbiter Laser Altimeter (LOLA) data: Spatial distribution and correlation with geologic features. *Icarus* **273**, 329–336 (2016).
- H. M. Jaeger, C.-H. Liu, S. R. Nagel, Relaxation at the angle of repose. *Phys. Rev. Lett.* **62**, 40–43 (1989).
- N. Gravish, D. I. Goldman, Effect of volume fraction on granular avalanche dynamics. *Phys. Rev. E Stat. Nonlin. Soft Matter Phys.* **90**, 032202 (2014).
- P. Tegzes, T. Vicsek, P. Schiffer, Development of correlations in the dynamics of wet granular avalanches. *Phys. Rev. E Stat. Nonlin. Soft Matter Phys.* **67**, 051303 (2003).
- F. Qian, T. Zhang, W. Korff, P. B. Umbanhowar, R. J. Full, D. I. Goldman, Principles of appendage design in robots and animals determining terradynamic performance on flowable ground. *Bioinspir. Biomim.* **10**, 056014 (2015).
- C. Li, P. Umbanhowar, H. Komsuoglu, D. E. Koditschek, D. I. Goldman, Sensitive dependence of the motion of a legged robot on granular media. *Proc. Nat. Acad. Sci. U.S.A.* **106**, 3029–3034 (2009).
- N. Mazouchova, P. B. Umbanhowar, D. I. Goldman, Flipper-driven terrestrial locomotion of a sea turtle-inspired robot. *Bioinspir. Biomim.* **8**, 026007 (2013).
- H. Marvi, C. Gong, N. Gravish, H. Astley, M. Travers, R. L. Hatton, J. R. Mendelson III, H. Choset, D. L. Hu, D. I. Goldman, Sidewinding with minimal slip: Snake and robot ascent of sandy slopes. *Science* **346**, 224–229 (2014).
- D. Andrews, A. Colaprete, J. Quinn, B. Bluethmann, J. Trimble, *Space 2015*, NASA Ames Research Center (American Institute of Aeronautics and Astronautics, 2015).
- B. Andreotti, Y. Forterre, O. Pouliquen, *Granular Media* (Cambridge University Press, 2009).
- B. McInroe, H. C. Astley, C. Gong, S. M. Kawano, P. E. Schiebel, J. M. Rieser, H. Choset, R. W. Blob, D. I. Goldman, Tail use improves performance on soft substrates in models of early vertebrate land locomotors. *Science* **353**, 154–158 (2016).
- B. Chong, Y. Ozkan Aydin, C. Gong, G. Sartoretti, Y. Wu, J. Rieser, H. Xing, J. Rankin, K. Michel, A. Nieceza, J. Hutchinson, D. Goldman, H. Choset, Coordination of back bending and leg movements for quadrupedal locomotion, in *Proceedings of Robotics: Science and Systems* (RSS, 2018); [www.roboticsproceedings.org/rss14/p20.html](http://www.roboticsproceedings.org/rss14/p20.html).
- Y. Ding, N. Gravish, D. I. Goldman, Drag induced lift in granular media. *Phys. Rev. Lett.* **106**, 028001 (2011).
- J.-Y. Wong, A. Reece, Prediction of rigid wheel performance based on the analysis of soil-wheel stresses: Part II. Performance of towed rigid wheels. *J. Terramechanics* **4**, 7–25 (1967).
- R. D. Maladen, Y. Ding, C. Li, D. I. Goldman, Undulatory swimming in sand: Subsurface locomotion of the sandfish lizard. *Science* **325**, 314–318 (2009).
- L. E. Silbert, D. Ertaş, G. S. Grest, T. C. Halsey, D. Levine, S. J. Plimpton, Granular flow down an inclined plane: Bagnold scaling and rheology. *Phys. Rev. E Stat. Nonlin. Soft Matter Phys.* **64**, 051302 (2001).
- T. Zhang, D. I. Goldman, The effectiveness of resistive force theory in granular locomotion. *Phys. Fluids* **26**, 101308 (2014).
- J. Y. Wong, *Terramechanics and Off-Road Vehicle Engineering: Terrain Behaviour, Off-Road Vehicle Performance and Design* (Butterworth-Heinemann, 2009).
- C. Creager, *Earth and Space 2012* (American Society of Civil Engineers, 2012).
- S. S. Sharpe, R. Kuckuk, D. I. Goldman, Controlled preparation of wet granular media reveals limits to lizard burial ability. *Phys. Biol.* **12**, 046009 (2015).
- N. Patel, R. Slade, J. Clemmet, The ExoMars rover locomotion subsystem. *J. Terramechanics* **47**, 227–242 (2010).
- C. C. Ward, K. Iagnemma, A dynamic-model-based wheel slip detector for mobile robots on outdoor terrain. *IEEE T. Robot.* **24**, 821–831 (2008).
- M. Sutoh, K. Nagaoka, K. Nagatani, K. Yoshida, Design of wheels with grousers for planetary rovers traveling over loose soil. *J. Terramechanics* **50**, 345–353 (2013).
- L. Crumpler, R. E. Arvidson, M. Golombek, J. A. Grant, B. L. Jolliff, D. W. Mittlefehldt; Athena Science Team, Rim structure, stratigraphy, and aqueous alteration exposures along Opportunity Rover’s traverse of the Noachian Endeavour crater, in *48th Lunar and Planetary Science Conference* (NASA Johnson Space Center, 2017).
- F. Qian, K. Daffon, T. Zhang, D. I. Goldman, *Nature-Inspired Mobile Robotics* (World Scientific, 2013), pp. 547–554.

**Acknowledgments:** We thank P. Umbanhowar for the helpful discussions, E. Aydin for the experimental assistance, and V. Margot Paez for the helpful discussion. Trade names and trademarks are used in this report for identification only. Their usage does not constitute an official endorsement, either expressed or implied, by the National Aeronautics and Space Administration. **Funding:** This work was supported by the Army Research Office (W911NF-18-1-0120) and the NASA National Robotics Initiative (NNX15AR21G). A.K. was partially supported by the President’s Fellowship of Georgia Institute of Technology. **Author contributions:** S.S. designed the Mini Rover and performed its experiments. A.K. performed single-wheel experiments and RFT model calculations. Y.O.A. constructed the fluidizing granular beds and aided in experimental design. R.P., W.B. (JSC-ER411), R.O.A. (JSC-ER111) facilitated on site RP15 experiments at JSC. A.K. and D.I.G. wrote the paper. **Competing interests:** The authors declare that they have no competing interests. **Data and materials availability:** All data needed to evaluate the conclusions in the paper are present in the paper or the Supplementary Materials.

Submitted 25 November 2019  
 Accepted 6 April 2020  
 Published 13 May 2020  
 10.1126/scirobotics.aba3499

**Citation:** S. Shrivastava, A. Karsai, Y. O. Aydin, R. Pettinger, W. Bluethmann, R. O. Ambrose, D. I. Goldman, Material remodeling and unconventional gaits facilitate locomotion of a robophysical rover over granular terrain. *Sci. Robot.* **5**, eaba3499 (2020).

## Material remodeling and unconventional gaits facilitate locomotion of a robophysical rover over granular terrain

Siddharth Shrivastava, Andras Karsai, Yasemin Ozkan Aydin, Ross Pettinger, William Bluethmann, Robert O. Ambrose and Daniel I. Goldman

*Sci. Robotics* **5**, eaba3499.

DOI: 10.1126/scirobotics.aba3499

### ARTICLE TOOLS

<http://robotics.sciencemag.org/content/5/42/eaba3499>

### SUPPLEMENTARY MATERIALS

<http://robotics.sciencemag.org/content/suppl/2020/05/11/5.42.eaba3499.DC1>

### RELATED CONTENT

<http://robotics.sciencemag.org/content/robotics/2/7/eaan5074.full>  
<http://robotics.sciencemag.org/content/robotics/4/34/eaax4316.full>

### REFERENCES

This article cites 24 articles, 6 of which you can access for free  
<http://robotics.sciencemag.org/content/5/42/eaba3499#BIBL>

### PERMISSIONS

<http://www.sciencemag.org/help/reprints-and-permissions>

Use of this article is subject to the [Terms of Service](#)

---

*Science Robotics* (ISSN 2470-9476) is published by the American Association for the Advancement of Science, 1200 New York Avenue NW, Washington, DC 20005. The title *Science Robotics* is a registered trademark of AAAS.

Copyright © 2020 The Authors, some rights reserved; exclusive licensee American Association for the Advancement of Science. No claim to original U.S. Government Works

## Supplementary Materials for

### **Material remodeling and unconventional gaits facilitate locomotion of a robophysical rover over granular terrain**

Siddharth Shrivastava, Andras Karsai\*, Yasemin Ozkan Aydin, Ross Pettinger,  
William Bluethmann, Robert O. Ambrose, Daniel I. Goldman\*

\*Corresponding author. Email: [daniel.goldman@physics.gatech.edu](mailto:daniel.goldman@physics.gatech.edu) (D.L.G.); [akarsai3@gatech.edu](mailto:akarsai3@gatech.edu) (A.K.)

Published 13 May 2020, *Sci. Robot.* **5**, eaba3499 (2020)  
DOI: 10.1126/scirobotics.aba3499

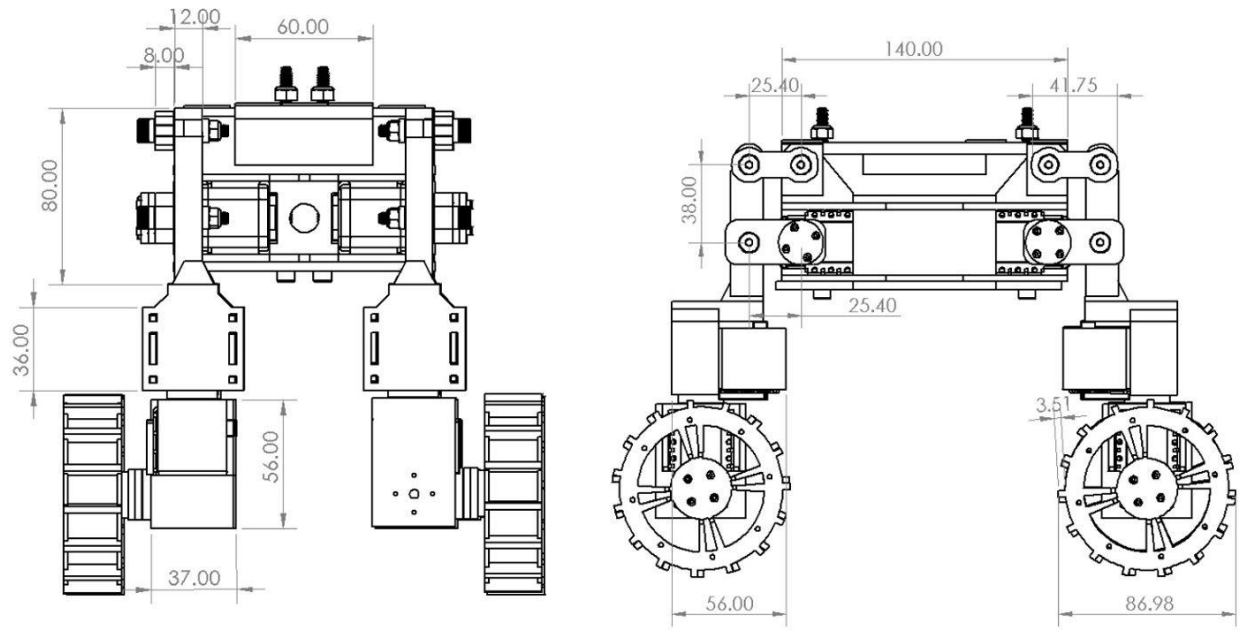
#### **The PDF file includes:**

Fig. S1. Engineering sketches of the Mini Rover.  
Fig. S2. Diagram of rover appendage actuations.  
Fig. S3. Granular experimentation bed and gantry.  
Fig. S4. Mini Rover RS gait velocity and sinkage profiles.  
Fig. S5. Dynamic reconfiguration with the RRP gait on various slopes.  
Legends for movies S1 to S9

#### **Other Supplementary Material for this manuscript includes the following:**

(available at [robotics.sciencemag.org/cgi/content/full/5/42/eaba3499/DC1](https://robotics.sciencemag.org/cgi/content/full/5/42/eaba3499/DC1))

Movie S1 (.mp4 format). RP15 climbs granular mound with the RS gait.  
Movie S2 (.mp4 format). Mini Rover using RS gait on a flat poppy seed bed.  
Movie S3 (.mp4 format). Mini Rover RS gait trial in granular experimentation bed.  
Movie S4 (.mp4 format). Single-wheel gantry trial of spin and sweep motion.  
Movie S5 (.mp4 format). Mini Rover RS gait trial measurement of drawbar force.  
Movie S6 (.mp4 format). Drawbar force measurements of RP15 prototype rover.  
Movie S7 (.mp4 format). Mini Rover RS gait drawbar force measurement in wet sand bed.  
Movie S8 (.mp4 format). Mini Rover RRP gait on sloped poppy seed bed.  
Movie S9 (.mp4 format). Comparison of Mini Rover RRP gait with wheel spin enabled versus disabled.



**Fig. S1. Engineering sketches of the Mini Rover.** Front view and side view engineering sketches of the Mini Rover. Dimensions are in millimeters.

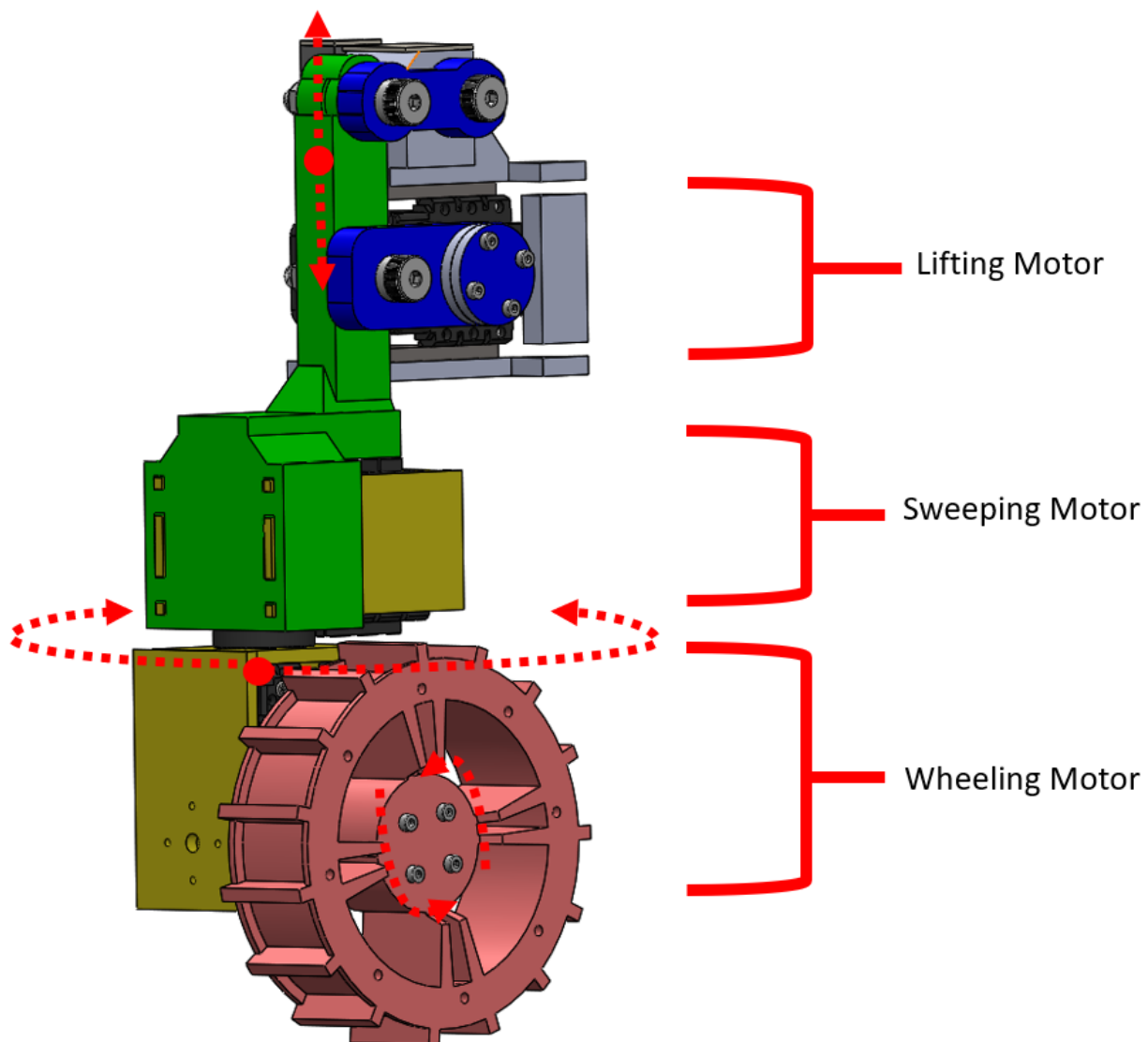


**Fig. S2. Diagram of rover appendage actuations.** Diagram of the lifting, sweeping, and wheeling motions of a single rover appendage.

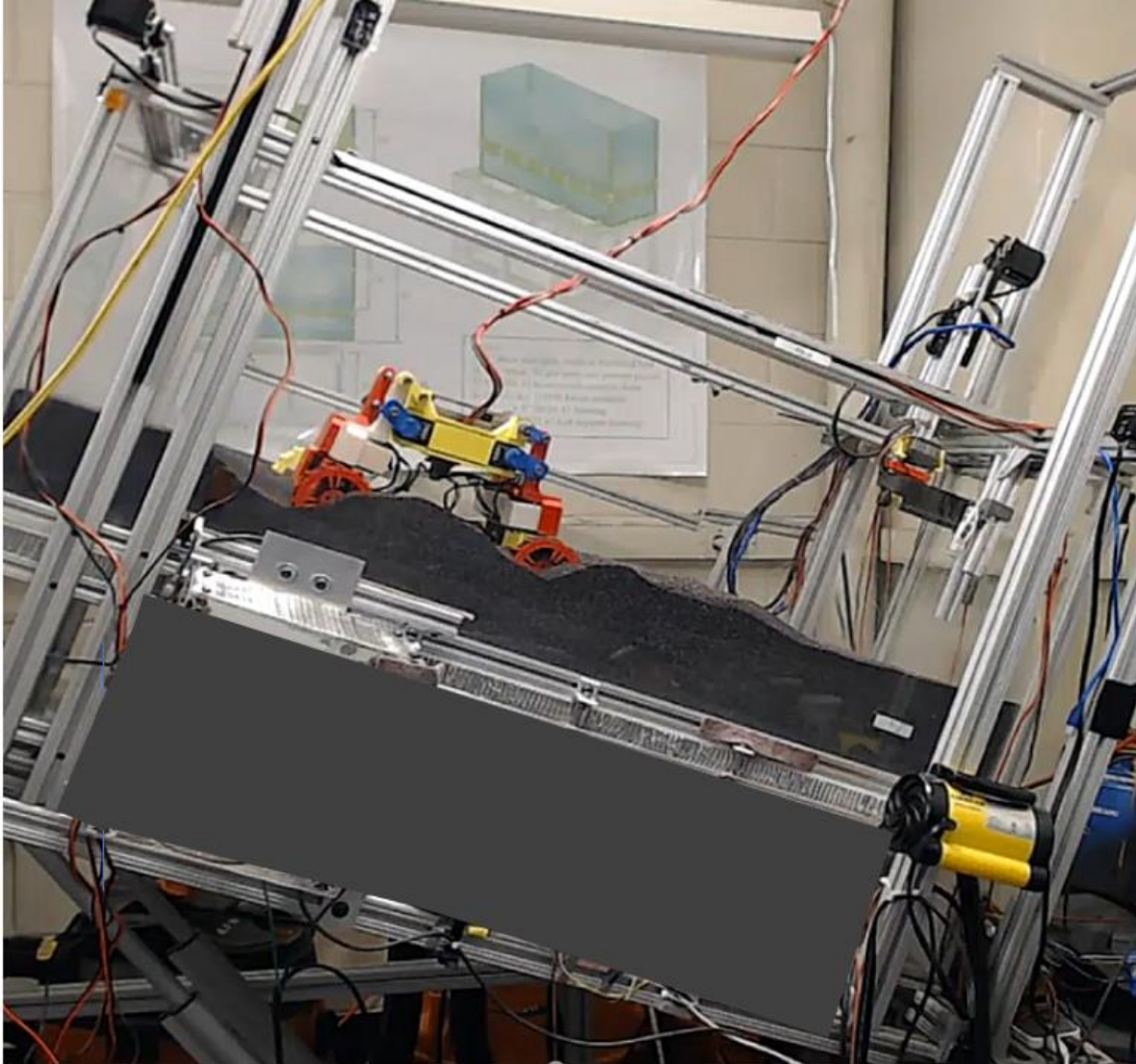


**Fig. S3. Granular experimentation bed and gantry.** Photograph of the complete granular experimentation bed with terrain fluidization, motion capture, and an automatic robot-reset gantry.

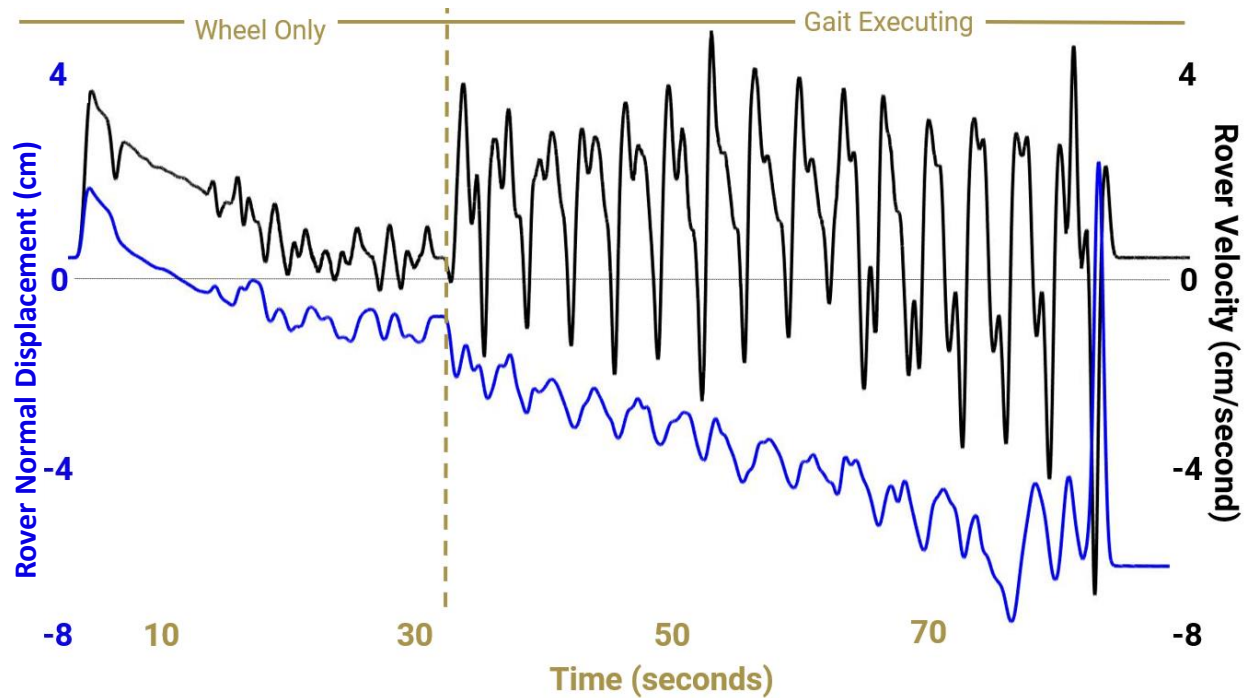


**Fig. S4. Mini Rover RS gait velocity and sinkage profiles.** Mini Rover displacement normal from the granular surface in the tilted frame from its initial position at rest (blue line, more negative values represent sinkage deeper into the material), along with Mini Rover velocity in the direction parallel to the granular bed (black line) as a function of time using the RS gait at  $\theta_{bed} = 15^\circ$ . From 0 to 30 seconds is the wheel only phase, then the RS gait initiates at the 30 second timestamp. The rover acts as a traditional wheeled vehicle while only wheeling prior to gait execution: the rover's slip increases and velocity decreases as the rover sinks deeper. However, the rover's slip and velocity become independent of the sinkage once the RS gait initiates. The rover continues sinking relative to the original terrain surface during the RS gait since it reconfigures the terrain by local avalanching, so it appears to continuously sink in the local tilted bed frame while actually climbing in the world frame.

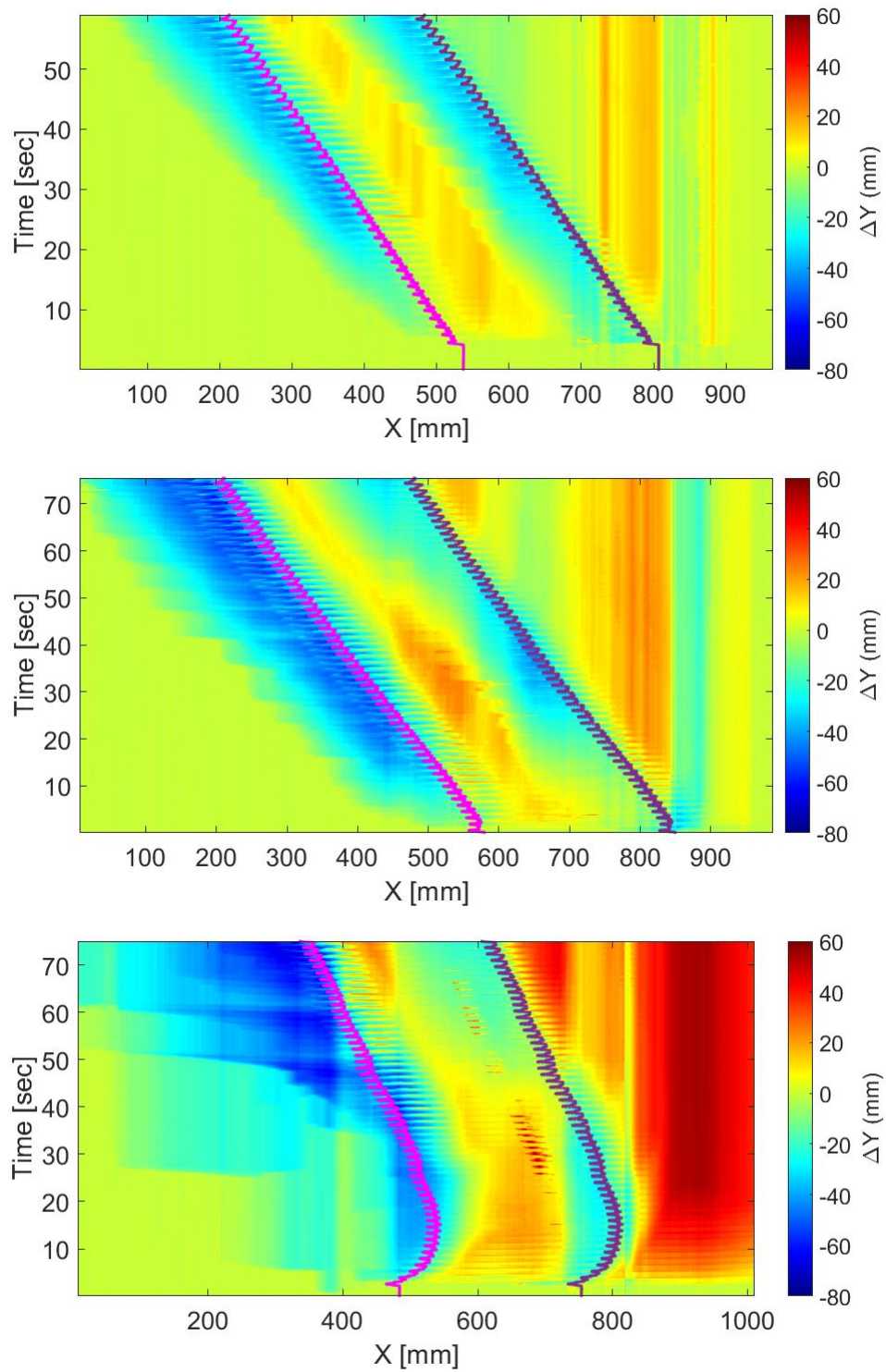


**Fig. S5. Dynamic reconfiguration with the RRP gait on various slopes.** Additional height difference colormaps of the granular media profiles over time as the Mini Rover executes the RRP gait for trials of  $\theta_{bed} = 15^\circ$  (top),  $20^\circ$  (middle),  $25^\circ$  (bottom), with the spatial

components in the tilted bed coordinate system. Magenta dots indicate the rover's front wheel's position over time, and purple dots indicate the rear wheel's position over time

#### **Movie S1. RP15 climbs granular mound with the RS gait.**

The RP15 prototype rover uses wheeled locomotion to traverse a sandy environment outdoors until it encounters a small mound of granular media. It then switches from wheeled locomotion to using the RS gait to climb over the mound. The footage is sped up from real time at 64x playback.

#### **Movie S2. Mini Rover using RS gait on a flat poppy seed bed.**

The Mini Rover (Fig. 1B) begins wheeled locomotion across a granular substrate of poppy seeds, experiences increasing slip, and entraps itself in the granular medium at  $\theta_{bed} = 0^\circ$ . The Mini Rover then begins executing the RS gait and restores locomotion. The footage is sped up from real time at 4x playback.

#### **Movie S3. Mini Rover RS gait trial in granular experimentation bed.**

Demonstrative trial of the Mini Rover's tilting and fluidizing granular bed. With the Mini Rover at rest, the bed first tilts to a chosen  $\theta_{bed}$ . The rover then executes its gait while the kinematic data is recorded. Afterwards, an overhead gantry picks up the Mini Rover with an electromagnet while the bed lowers down until it has zero tilt. The bed then fluidizes the granular media for a short time with air blowers to reset the granular state, and the Mini Rover is placed back into a set position by the gantry. The footage is sped up from real time at 10x playback.

#### **Movie S4. Single-wheel gantry trial of spin and sweep motion.**

Demonstrative trial of the single wheel gantry (Fig. 2A) tilting, fluidizing, and executing a commanded trajectory for a trial of  $\theta_{bed} = 10^\circ$  and  $v_x = 11 \text{ mm/s}$ . The footage is sped up from real time at 4x playback.

#### **Movie S5. Mini Rover RS gait trial measurement of drawbar force.**

The Mini Rover executing the RS gait for a drawbar force measurement trial at  $\theta_{bed} = 0^\circ$  (Fig. 3A). The footage is sped up from real time at 16x playback.

#### **Movie S6. Drawbar force measurements of RP15 prototype rover.**

RP-15 drawbar experiments at Johnson Space Center (Fig. 3D). The trial with the green box illustrates RP-15 wheeling, transitioning to the RS gait, then terminating the experiment. The trial with the red box illustrates RP-15 wheeling only then terminating the experiment. The graph (left) plots the drawbar corresponding to either trial (right).

#### **Movie S7. Mini Rover RS gait drawbar force measurement in wet sand bed.**

The Mini Rover executes the RS gait in a bed of wet sand for a drawbar force measurement trial at  $\theta_{bed} = 0^\circ$ . The footage is sped up from real time at 2x playback.

**Movie S8. Mini Rover RRP gait on sloped poppy seed bed.**

The Mini Rover executes the RRP gait as defined in Fig. 4 on the granular bed at  $\theta_{bed} = 20^\circ$ . It uses the granular conveyance and avalanching mechanisms described in the main text to ‘swim’ up the steep slope of granular media. The footage is sped up from real time at 16x playback.

**Movie S9. Comparison of Mini Rover RRP gait with wheel spin enabled versus disabled.**

Comparison of the Mini Rover’s RRP gait at  $\theta_{bed} = 25^\circ$  with wheel spinning enabled vs. disabled (Fig. 4D). The footage is sped up from real time at 16x playback.